




Repeated Cyclogenesis on Hot-Exoplanet Atmospheres with Deep Heating

Jack W. Skinner^{1,2*}, Joonas Nättälä^{3,4†}, James Y-K. Cho^{2,3‡}

¹ *California Institute of Technology, 1200 East California Boulevard, Pasadena, California 91125, USA*

² *Martin A. Fisher School of Physics, Brandeis University, 415 South Street, Waltham, Massachusetts 02453, USA*

³ *Center for Computational Astrophysics, Flatiron Institute, 162 Fifth Avenue, New York, New York 10010, USA and*

⁴ *Physics Department and Columbia Astrophysics Laboratory, Columbia University, 538 West 120th Street, New York, New York 10027, USA*

Most current models of hot-exoplanet atmospheres assume shallow heating, a strong day-night differential heating near the top of the atmosphere. Here we investigate the effects of energy deposition at differing depths in a model tidally locked gas-giant exoplanet. We perform high-resolution atmospheric flow simulations of hot-exoplanet atmospheres forced with idealized thermal heating representative of shallow and deep heating (i.e., stellar irradiation strongly deposited at $\sim 10^3$ Pa and $\sim 10^5$ Pa pressure levels, respectively). Unlike with shallow heating, the flow with deep heating exhibits a new dynamic equilibrium state, characterized by repeated generation of giant cyclonic storms that move away westward once formed. The formation is accompanied by a burst of height-ened turbulence, leading to the production of small-scale flow structures and large-scale mixing of temperature on a timescale of ~ 3 planetary rotations. Significantly, while effects that could be important (e.g., coupled radiative flux and convectively excited gravity waves) are not included, over a timescale of several hundred days the simulations robustly show that the emergent thermal flux depends strongly on the heating type and is distinguishable by current observations.

Introduction.— Current and upcoming space-based missions, such as the James Webb Space Telescope (JWST) [1] and Ariel [2], will enable next-generation observations of exoplanet atmospheres. However, accurate dynamics modeling is required to interpret and guide these observations. At present, most general circulation simulations of 1:1 spin-orbit synchronized hot-exoplanet atmospheres are performed with a strong day-night differential heating near the top of the modeled atmosphere [3–15]. Here we refer to this type of heating as *shallow heating*. Importantly, *deep heating*—i.e., a strong day-night differential heating at a much greater depth, in addition to near the top—has also been suggested in the past [7, 16–19]. Such variations in the energy deposition depth can be due to, e.g., changes in how the incoming stellar radiation is transferred, reflected, or absorbed by the planet’s atmosphere. In addition, a preliminary modeling of the recent JWST observation of the hot-exoplanet WASP-96 b also suggests a deep heating for this planet [20]. For exoplanets, the atmospheric response to such differences in heating is still not well understood [21, 22]; hence, a robust study of the response is needed, for both theory and observation. In this Letter we investigate the dynamical consequence of deep heating—specifically, stellar irradiation deposited at the pressure level of $\sim 10^5$ Pa, as well as at $\sim 10^3$ Pa—on hot-exoplanet atmospheres with a three-dimensional (3D), global hydrodynamics model.

In the case of the Earth, for which ample observations and modeling studies exist, it is well known that temperature profiles resulting from heating at different pressure levels (depths) lead to different large-scale dynamics. This is due to, inter alia, thermal-mechanical forcing of

lateral motion and entrainment/detrainment; see, e.g., [23–26], and references therein. Likewise, the equilibrium temperature distribution $T_e(\lambda, \phi, p, t)$ is a key factor that governs the large-scale dynamics on exoplanets; here λ, ϕ, p are the longitude, latitude, and pressure, respectively; and, T_e is generally dependent on time t , as indicated. Under 1:1 spin-orbit synchronization, in the absence of atmospheric motion, a permanent dayside and nightside is expected on the planet—especially at low p -levels. However, dynamics can subvert this expectation [6, 11, 13–15, 27–29]. For example, with deep heating, heavier masses of atmospheric fluid can be energized because of stratification [27] and stronger upwardly-propagating internal gravity waves are excited [28]. Both mechanisms can smooth, or even reverse, the dayside-nightside temperature gradient via advection and wave-mean flow interaction. In this way, dynamics is crucial in configuring the temperature field, in both space and time—and ultimately what is observed.

Numerical Simulation.— The global dynamics, and its associated temperature distribution, of hot-exoplanet atmospheres are simulated by solving the primitive equations (PEs) in the vorticity-divergence-potential temperature form [30, 31]

$$\begin{aligned} \frac{\partial \zeta}{\partial t} &= \mathbf{k} \cdot (\nabla \times \mathbf{n}) \\ \frac{\partial \delta}{\partial t} &= \nabla \cdot \mathbf{n} - \nabla^2 \left(\frac{1}{2} \mathbf{v}^2 + \Phi \right) \\ \frac{\partial \Theta}{\partial t} &= -\nabla \cdot (\Theta \mathbf{v}) - \frac{\partial}{\partial p} (\omega \Theta) + \frac{\dot{q}_{\text{net}}}{\Pi}, \end{aligned} \quad (1)$$

where decreasing p is the increasing vertical coordinate, $\zeta \equiv \mathbf{k} \cdot \nabla \times \mathbf{v}$ and $\delta \equiv \nabla \cdot \mathbf{v}$ are the vorticity and divergence

of the horizontal velocity field $\mathbf{v}(\lambda, \phi, p, t)$, respectively, and $\Theta \equiv (c_p/\Pi)T$ is the potential temperature—related to the entropy s by $ds = c_p d(\ln \Theta)$. Here \mathbf{k} is the local vertical direction (magnitude of unity); ∇ is the horizontal gradient operator on constant p -surfaces; c_p is the specific heat capacity at constant p ; $\Pi \equiv c_p (p/p_0)^{\mathcal{R}/c_p}$ is the Exner function, where p_0 is a constant reference pressure ($\equiv 10^6$ Pa in this work) and \mathcal{R} is the mean specific gas constant; and, $T(\lambda, \phi, p, t)$ is the ordinary temperature field. Also, $\mathbf{n} \equiv -(\zeta + f)\mathbf{k} \times \mathbf{v} - \delta \mathbf{v} - \partial(\omega \mathbf{v})/\partial p$, where f is the Coriolis parameter and $\omega \equiv dp/dt$ is the vertical velocity; Φ is the geopotential; and, $\dot{q}_{\text{net}}(T_e)$ is the net heating rate field, the key element in this work.

The Eq. (1) set is closed with the following relationships: $\partial\Phi/\partial\Pi = -\Theta$, $\partial\omega/\partial p = -\delta$, and $p = \rho RT$, where ρ is the density field. The boundary conditions at the top and bottom of the domain are free-slip—i.e., $\omega = 0$. As for the lateral direction, the fields are periodic in λ , and $\mathbf{v} \cos \phi$ mapping is used to represent \mathbf{v} in terms of the scalar Legendre expansions. The latter is convenient for solving the equations [30] and forces $\mathbf{v} \cos \phi$ to be null at the poles.

The full set of PEs is solved with a well-tested pseudospectral code employing hyperviscosity [11, 31, 32]. The results are based on numerically converged, as well as consistent, simulations [33] at very high resolution—i.e., a horizontal resolution of up to T1365 (corresponding to a truncation of 1365 total modes and 1365 azimuthal modes in the Legendre expansion) and with a vertical resolution of up to L200 (corresponding to 200 layers in p -space) at T682 resolution. A snapshot from a sample T1365L20 solution is presented in Fig. 1. Note the intricate folding and layering of fine-scale fronts around the large organized ζ and T areas, which are constantly in motion; note also the close relationship between the flow and temperature. The fine-scale structures, which cannot be captured without high resolution and low dissipation, are paramount for accurate numerical solutions and observation interpretations [32]. Other important numerical parameters, along with their values, and convergence tests of the simulations are provided in the Appendixes; see also Refs. [11], [31], and [32] for broader comparisons.

In this Letter we discuss two exoplanets, HD209458 b and WASP-96 b. Although the precise shape of temperature profiles for any exoplanet is currently unknown, the two serve as fiducial examples of exoplanets with atmospheres characterized by shallow heating and deep heating, respectively [3, 20]. Apart from the profiles, they possess physical parameter values that are effectively the same, from an atmospheric dynamics standpoint. Hence, they permit the effects of heating type on the dynamics to be well-delineated. The relevant physical (orbital and atmospheric) parameters, and their values, are also given in the Appendixes. The characteristic advection time, $\tau_a \equiv R_p/U$, is similar for both planets; here R_p is the planetary radius and U ($\sim 10^3$ m s $^{-1}$) is the characteristic

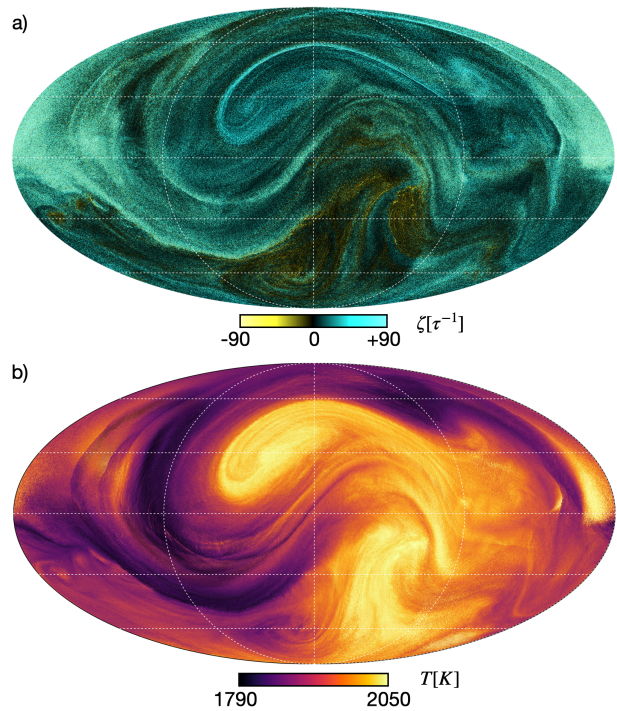


FIG. 1. Vorticity ζ and temperature T fields (a and b, respectively) with deep heating at time $t = 155$ and at the 10^5 Pa pressure level. The generic response to deep heating is large-scale vortices rolling up, breaking off, and then moving westward away from the point of formation at mid-latitudes. The point may be slightly shifted in longitude at other times or in simulations with slightly different numerical parameters; a movie is available [34].

speed of a structure of length scale R_p . Additionally, for large portions of the atmosphere on both planets $\tau_a \ll \tau$, where τ is the planetary rotation period. From hereon time is given in terms of τ .

The salient difference between the two planets is the strength (amplitude and timescale) of the thermal forcing in the deep region of their atmospheres—i.e., at p -levels between $\sim 5 \times 10^4$ Pa and $\sim 5 \times 10^5$ Pa. Fig. 2 shows the model $T(p)$ profiles for the planets, these are derived from one-dimensional (1D) radiative transfer calculations that incorporate Spitzer and Hubble observations [3, 16, 35]; all profiles represent stable stratification throughout the modeled atmosphere. In this work, both atmospheres are driven purely by a thermal relaxation to a prescribed temperature distribution ($\propto \cos \lambda \cos \phi$ on the dayside and uniform on the nightside) and on a timescale τ_r ($\propto p/T_e^4$) [36]. Although highly idealized, the forcing is reasonable—particularly for the deep region [29]. Note that, in the deep region $\tau_r/\tau_a \gtrsim 1$ for HD209458 b [9, 11, 27] whereas $\tau_r/\tau_a \lesssim 1$ for WASP-96 b; in the upper region (i.e., $p \lesssim 10^4$ Pa), $\tau_r/\tau_a \ll 1$ for both planets. The larger dayside–nightside T difference and shorter τ_r in the deep region of WASP-96 b lead to a significant difference in the flow and temperature distributions, as shown below.

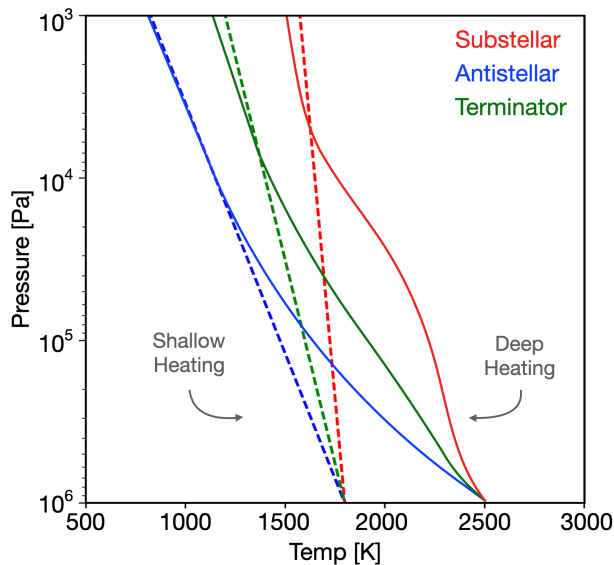


FIG. 2. Temperature profiles $T(p)$ of shallow heating (dashed lines) and deep heating (solid lines). Colors refer to different points in longitude. The dayside–nightside difference is larger and the thermal relaxation time is smaller in the deep region for deep heating.

Modon Pair with Shallow Heating.— On 1:1 spin–orbit synchronized hot-exoplanets, the intense irradiation from their host stars creates flow structures on a wide range of scales and amplitudes [13, 32]. These include planetary-scale vortex-couplets, small-scale vortex singlets, large-amplitude Rossby waves, and meso-scale gravity waves [11, 13, 27, 28]. They are generic to planets with strong dayside–nightside differential heating mostly in the upper region [6, 32].

Under shallow heating, giant modons—vortex couplets with their constituent vortices having opposite signs of vorticity [37]—are the preeminent structures that emerge in the flow; see Fig. 3a. Generally, there are two of them—a modon and an antimodon (composed of two cyclones and two anticyclones that initially span across the equator, respectively): a cyclone is a vortex with $\zeta \cdot \Omega > 0$ and an anticyclone is a vortex with $\zeta \cdot \Omega < 0$, where $\zeta = \zeta \mathbf{k}$ and Ω is the planetary rotation vector that orients the north pole. These long-lived, non-stationary structures are responsible for transporting and mixing hot and cold patches of the atmosphere, in their cores as well as in their interstitial areas. In this way, they induce distinct time-varying thermal signatures that could be observable [13, 14, 27]. Here small-scale flow structures are important because they perturb the giant modons from stationary or smoothly-translating states, seen in lower resolution or more dissipative simulations [32]. In general, modons move chaotically, due to the continual nonlinear interactions with the small-scale structures [14]. Over long duration, the flow evolution exhibits several equilibrium states, with occasional sudden transitions between them [13]. These states are: *i*) steadily

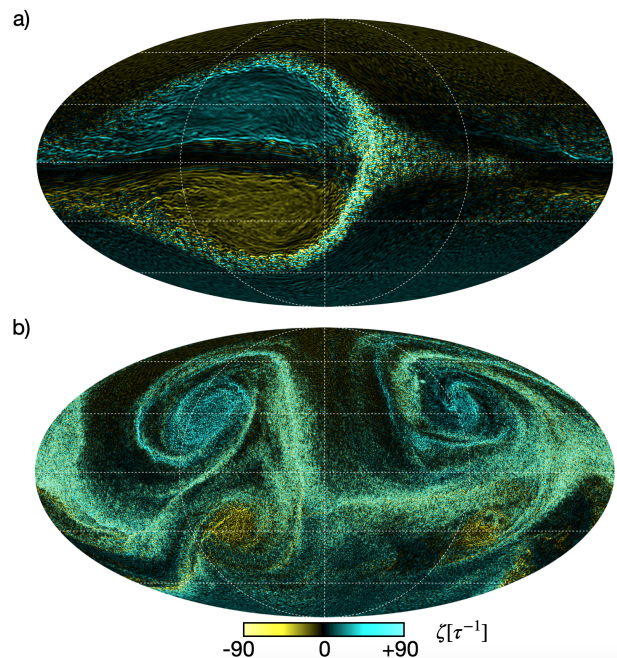


FIG. 3. ζ fields at the 10^5 Pa level with shallow and deep heating (a and b, respectively), showing the flows dominated by different organized structures (after $t \approx 10$). In a) the flow is dominated by a modon and a much weaker antimodon, whereas in b) the flow is dominated by a quartet of cyclones in a von Kármán vortex street-like formation. In the latter, the cyclone quartet exhibits a quasi-periodic life cycle (of period ~ 10) that begins with the flow similar to that seen in Fig. 1a.

translating, *ii*) oscillatory, and *iii*) vortex-street-like.

In state *i*), a strong modon and a much weaker antimodon form in the deep region near the substellar and antistellar points, respectively. Both couplets eventually drift westward after an initial eastward translation by the modon. Subsequently, one or both may spread apart or entirely break up repeatedly near the eastern terminator. In state *ii*), the two cyclones of the modon spin out alternatively in the northern and southern hemispheres, both moving off to the west after spinning out. This leads to a noticeable symmetry breaking between the two hemispheres. Importantly, this state is transient, lasting a much shorter duration than the other states. In state *iii*), cyclones straddle a large-amplitude equatorial Rossby wave and steadily translate westward with the wave in a von Kármán vortex street-like chain [38]—without breaking up. This state is generally seen in the very deep regions ($p \gtrsim 10^6$ Pa), post a very long build-up period (typically $t \sim 200$) [13].

Cyclone Quartet with Deep Heating.— Fig. 3b shows the ζ field for WASP-96 b at $t = 157$ (at the same p -level of the fields in Fig. 1). Fig. 3b should be compared with Fig. 1a, as the two give an idea of the dynamic and quasi-cyclic nature of the flow with deep heating: they illustrate roughly the half points of a cycle. That is, the field shown in Fig. 3b is essentially the same as that at

$t \approx 145$ (as well as at $t \approx 15$), and the field shown in Fig. 1a is essentially same as that at $t \approx 165$ (albeit with $\sim 45^\circ$ westward shift in the latter).

In general, the flow contains a much greater number of small-scale vortices at the shown p -level than that with shallow heating (cf. Fig. 3a and Fig. 3b). More importantly, unlike in simulations with shallow heating, large uncoupled cyclones—usually four of them—repeatedly form and individually spin off westward at mid-latitudes. This occurs after an initial brief period of a giant cyclonic modon formation, subsequent rapid eastward translation, and total breakup on the dayside ($t \lesssim 10$). After the breakup, large cyclones form via Rossby wave breaking in both the northern and southern hemispheres: the wave breaks in the counter-clockwise and clockwise directions in the northern and southern hemispheres, respectively, rolling up into cyclones. The growth time for the formation is very short (~ 1); but, once formed, the cyclones last for a period of ~ 3 to ~ 15 , before succumbing to large-scale external straining. The signature of the cyclone quartet life cycle can be seen in disk-integrated thermal flux, as discussed below. The copious small-scale vortices (storms), continuously regenerated in bursts and generally populated along the sharp fronts surrounding the cyclones, also remain coherent for a long time ($\gtrsim 10$).

The recurring cyclogenesis and bursts of turbulence vigorously mix the atmosphere and homogenize the planet’s T field over short timescales (~ 3); see Fig. 4—in particular, the much smaller peak amplitudes compared to those for the shallow heating case. The geneses and bursts cause the hot and cold patches of the atmosphere to be highly variable in space and time. While the flow of state ii) with shallow heating is moderately similar, that flow is much less dynamic (with greatly reduced U and turbulence) and occurs at much greater depths (i.e., $p \gtrsim 10^6$ Pa) [13]. This is due to the markedly different forcing amplitude and relaxation timescale in the deep region between the two types of heating, as they power different mechanisms for vortex formation (e.g., barotropic instability with shallow heating and baroclinic instability [39] with deep heating).

Most importantly, this “cyclogenesis plus enhanced turbulence” state is the *sole* equilibrium state exhibited with deep heating—i.e., multiple equilibrium states are not exhibited, as with shallow heating. Additionally, with shallow heating, a weak antimodons initially forms in the region $p \lesssim 2.5 \times 10^4$ Pa (see Fig. 4 of Ref. [14]); a much weaker, antisymmetric version of this structure is present with shallow heating on the nightside and together constitute a pair of heton quartets [40]. After its formation, the cyclonic modon slowly becomes more columnar (barotropic) over time. However, with deep heating, the four cyclones are strongly barotropic (extending essentially over the entire region above $p \approx 10^5$ Pa) from the time they first begin to emerge at $t \approx 10$. After $t \approx 17$, the cyclones are repeatedly generated through

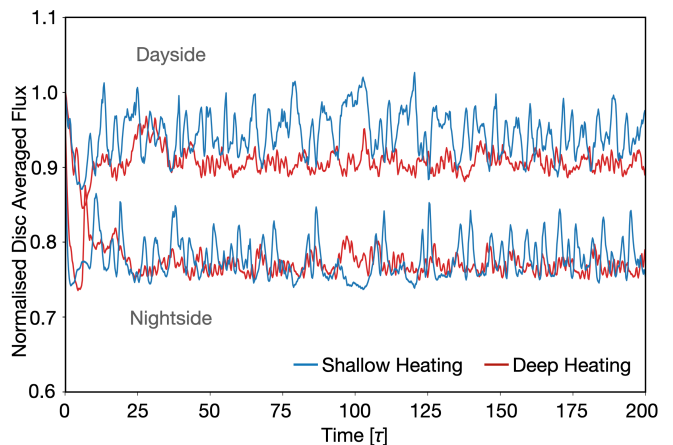


FIG. 4. Time-series of disk-averaged thermal flux ($\propto \sigma T^4$, where σ is the Stefan–Boltzmann constant) at the $p = 10^5$ Pa level, with disks centered on the dayside (top) and nightside (bottom), for atmospheres with shallow heating (blue) and deep heating (red). Each series is normalized by the initial terminator value at the $p = 10^5$ Pa level.

out the simulation duration ($t = 300$ here and longer at lower resolutions). We emphasize that baroclinic instability mainly powers the cyclone generation; overall, the flow is strongly barotropic.

Given the marked difference in behavior, the type of heating on hot-exoplanets could be constrained by current observations. Consider, for example, the time series of disk-averaged thermal flux, corrected with a cosine projection factor for the geometry. Four series are shown in Fig. 4, with the disks centered on the antistellar and substellar points (labeled nightside and dayside, respectively). The nightside series corresponds to the flux at the peak primary eclipse, and the dayside series corresponds to the flux just before ingress or after egress of the secondary eclipse. The series are from the simulations presented in Fig. 3 with the shallow heating case in blue and the deep heating case in red.

In both cases, the motion of large storms around the planet leads to flux peaks that are roughly 180° out of phase at the dayside and the nightside. However, as already noted, the amplitude of the peaks is significantly reduced with deep heating compared to those with shallow heating. This difference arises because the average over the disk is modulated by the homogeneity of the T field, caused by the mixing. With deep heating, hot and cold patches periodically peel away westward from their points of emergence on the dayside and nightside, respectively—often past the terminators. This results in a flux series with a lower amplitude and higher frequency peaks. At $p \sim 10^5$ Pa, the hottest patch of the atmosphere is generally situated near the substellar point on the dayside, and even slightly shifted eastward at times; storms that spin off do sequester and transport hot temperatures towards the western terminator at mid-high latitudes but, tempered by the viewing geometry, do not

contribute significantly to the disk-averaged flux centered on the substellar point. Superficially, this behavior appears similar to that reported in past simulations employing shallow heating and low resolution; however, the behavior here is much more dynamic and is generated by a completely different mechanism. With shallow heating, hot patches advected by a modon moving quasi-periodically around the planet over a longer period lead to high-amplitude and lower frequency peaks in the flux. As a consequence, the shallow heating case would appear to have a more westward shifted “hot spot” than the deep heating case. Note that the difference in the peaks between the two types of heating (~ 100 K, or $\sim 4\%$ of the prescribed temperature at the substellar point) is greater than the expected accuracy of JWST measurements, which is ≈ 30 K [41, 42].

Discussion.— In this letter we investigate the effects of different depths of heating on the atmospheric dynamics of exoplanets. Two generic types of heating are heuristically designated as “shallow heating” and “deep heating”. While we remain agnostic on the exact origin of the energy deposition variations, we note that such changes are naturally expected, e.g., due to changes in how the host star radiation is transferred and absorbed in the planet’s outer layers. Such changes are further amplified by the unknown vertical distribution of clouds and aerosols in the atmosphere. Interestingly, both types of heating are consistent with temperature profiles obtained by 1D radiative transfer calculations utilizing Spitzer, Hubble, and JWST observations [18, 19, 35, 43].

Here, the focus is laid on the influence of the deep heating—particularly on the large-scale atmospheric dynamics and its associated temperature redistribution in the modeled region, $p \in [10^3, 10^6]$ Pa. In the past, most simulations have employed shallow heating only. Some physical mechanisms that may influence the dynamics and temperature (e.g., the radiative flux feedback from temperature redistributions and saturation of upwardly propagating gravity waves excited by convection below) have not been included; but, they are not expected to qualitatively change the main result reported here because of the duration and vertical range of the simulations ([21], and references therein).

The main result here is that, with deep heating, a new persistent flow state arises in which giant cyclones repeatedly form near the substellar point and move away westward. The formation and subsequent motion redistribute the temperature more homogeneously over the planet, compared with the shallow heating case. Importantly, the cyclones—generally a quartet of them—are accompanied by bursts of heightened turbulence activity. This enhances the mixing of large hot and cold areas of the atmosphere. Moreover, unlike with shallow heating, this is the sole equilibrium state exhibited with deep heating; with shallow heating, a multitude of states is exhibited.

The new, exclusive state exhibited in the flows driven by deep heating is characterized by disk-averaged temperature fluxes which are overall less variable, particularly near $p = 10^5$ Pa. These fluxes are lower in amplitude, compared with those generated by flows driven by shallow heating. More specifically, the typical difference in the flux is $\sim 10\%$. This is produced by a disk-averaged temperature difference of $\mathcal{O}(10^2$ K) between the atmospheres with the two types of heating. In addition to the amplitude difference, the thermal flux also exhibits markedly different temporal behavior for the two types of heating; for example, the fluxes for deep heating contain higher frequency perturbations, compared with those for shallow heating. Such differences are distinguishable by next-generation telescopes such as the JWST [1] and Ariel [2]. Therefore, the two types of heating can be clearly delineated by current observations.

Acknowledgements.— The authors thank Quentin Changeat for helpful discussions. J.W.S thanks the Jet Propulsion Laboratory, California Institute of Technology, where some of this work was completed under a contract with the National Aeronautics and Space Administration (80NM0018D0004). J.N is supported by a joint Columbia University and Flatiron Institute Research Fellowship. The Flatiron Institute is acknowledged for providing computational resources and support. This work resulted from an initial discussion at the Exoplanet Symposium 2022, organized at the Flatiron Institute.

* jskinner@caltech.edu

† jnattila@flatironinstitute.org

‡ jamescho@brandeis.edu

A. Numerical Model

In this work, we employ the pseudospectral code used in Refs. [13, 31, 32] to simulate the atmospheric dynamics of tidally synchronized hot-exoplanets, HD209458 b and WASP-96 b. In this section, we provide additional technical information pertaining to the simulations. More details are given in Refs. [31, 32]. The code solves the hydrostatic primitive equations in vorticity–divergence–potential temperature form [30] using pressure p as the vertical coordinate. The equations governing the dynamics are integrated on a sphere providing natural boundary conditions in the horizontal (λ, ϕ) directions (where λ is the longitude and ϕ is the latitude). In the vertical direction, we employ the free-slip condition (i.e., $Dp/Dt = 0$, where D/Dt is the material derivative) at the top and bottom p -surfaces.

The initial condition and thermal forcing employed in the HD209458 b simulations are the same as in previous works [11, 14, 32]. The flow is forced with a Newtonian relaxation scheme [36], which relaxes the terminator temperature distribution (given by the average of the substellar and antistellar equilibrium temperatures) to the specified equilibrium temperature distribution. The substellar, antistellar, and terminator profiles, all as functions of p , are as shown in Fig. 2 of the main text. These profiles are derived from radiative transfer calculations of WASP-96 b [20] and HD209458 b [3]. The timescale for radiative cooling $\tau_{\text{rad}}(p)$ is computed from for each of the terminator profiles following [29]; $\tau_{\text{rad}}(p)$ ranges from $\mathcal{O}(10^6 \text{ s})$ at $p = 10^6 \text{ Pa}$ to $\mathcal{O}(10^4 \text{ s})$ at $p = 10^3 \text{ Pa}$. We have verified that the profiles we use are stably stratified by computing the Brunt-Väisälä frequency \mathcal{N} and confirmed that $\mathcal{N}^2 > 0$ throughout the simulation domain.

B. Physical and Numerical Parameters

The physical parameters for the two planets discussed in the main text are summarized in Table I. Additional parameters for these planets can also be found in Refs. [44] and [6], respectively. Numerical parameters for the simulations of WASP-96 b and HD209458 b are summarized in Table II.

In this work, we denote the simulation resolution (e.g., T341L200) by the “T number” for the horizontal resolution, which is the truncation wavenumber in the spherical harmonic expansion, and the “L number” for the vertical resolution, which is the number of (linearly spaced) layers in the p -space. Regarding the latter, p_t (always set to be 0) and p_b are the top and bottom boundaries of the computational domain, respectively. The prognostic variables (vorticity, divergence, and potential temperature) are defined on “1/2-layers”, referred to as active layers. Hence, \tilde{p}_t and \tilde{p}_b , which are the topmost and bot-

Parameter	HD209458b	WASP-96b	Units
Rotation period τ	84.0	81.6	hours
Rotation rate Ω	2.08×10^{-5}	2.14×10^{-5}	s^{-1}
Radius R_p	1.00×10^8	8.58×10^7	m
Mass M_p	1.31×10^{27}	9.11×10^{26}	kg
Surface gravity g	10.0	8.27	ms^{-2}
Specific gas const. \mathcal{R}	3.50×10^3	3.50×10^3	$\text{J kg}^{-1} \text{K}^{-1}$
Specific heat const. c_p	1.23×10^4	1.23×10^4	$\text{J kg}^{-1} \text{K}^{-1}$
$T_{\text{SS}} (T_{\text{AS}})$ at 10^3 Pa	1570 (820)	1550 (820)	K
$T_{\text{SS}} (T_{\text{AS}})$ at 10^6 Pa	1800 (1800)	2500 (2500)	K

TABLE I. Physical parameters of the exoplanets, HD209458 b and WASP-96 b, used for the simulations in the main text.

tommost active levels, are independently varied while p_t and p_b enforce the free-slip boundary conditions.

The generalized diffusion operator $\nabla^{2\mathbf{p}}$ depends on the order \mathbf{p} ; here $\mathbf{p} = 1$ is the usual Laplacian operator and $\mathbf{p} = 8$, for example, is the 16th-order hyper-viscosity operator [45]. The operator is accompanied by the related viscosity coefficient $\nu_{2\mathbf{p}}$ multiplying the operator. Lastly, we use a Robert–Asselin filter [46] with coefficient ϵ [47].

The simulations discussed in the main text are of resolution T1365L20 with $\tilde{p}_t = 5 \times 10^3 \text{ Pa}$, $\tilde{p}_b = 1 \times 10^6 \text{ Pa}$, $\Delta t = 4.5 \text{ s}$, $\mathbf{p} = 8$, $\nu_{16} = 3.5 \times 10^{-53} R_p^{16} \tau^{-1}$, and $\epsilon = 0.02$. The duration for the simulations is 300τ , long enough for the system to reach quasi-equilibrium and exhibit more than 10 cycles of cyclone generation thereafter. We have verified that the flow evolution in the simulations is qualitatively the same as those in longer duration simulations, at lower horizontal resolutions—i.e., 500τ and 1000τ at T682L50 and T341L200, respectively.

C. Convergence Tests

The simulations in this work have been extensively tested and verified for numerical consistency and convergence. By varying all the parameters listed in Table II, the results have been verified to remain qualitatively unchanged. Specifically, we have performed effectively identical (i.e., numerically equatable) simulations with increasing horizontal resolution, to confirm that the features of the flow remain qualitatively the same. We note that the solutions are converged only at T341L10 resolution [32]. We have also verified that the primary conclusions do not change when \tilde{p}_t and \tilde{p}_b are independently varied while keeping L per Pa constant; see Table II. In particular, we have verified that varying \tilde{p}_b away from 10^6 Pa , the level to which the thermal forcing extends, does not qualitatively change the salient features of the flow and temperature fields discussed in the main

Parameter	Value
Horizontal resolution T	{341, 682, 1365}
Vertical resolution L	{3, 10, 20, 50, 100, 200}
Top active p -level \tilde{p}_t [10^3 Pa]	{1, 5, 10}
Bot. active p -level \tilde{p}_b [10^5 Pa]	{1, 2, 5, 10, 20}
Timestep size Δt [s]	{12, 6, 4.5}
Viscosity order \mathbf{p}	{1, 2, 4, 8, 16}
ν_{16} viscosity coeff. [$R_p^{16} \tau^{-1}$]	{ 10^{-48} , 10^{-51} , 10^{-53} }
Robert-Asselin coeff. ϵ	{0.002, 0.02, 0.2}

TABLE II. Range of numerical parameters for the simulations in this work.

text (e.g., cyclone generation, thermal waves, and sharp fronts). Varying \tilde{p}_t away from 5×10^3 Pa, roughly the level to which simulations typically extend [9, 11, 31, 32], also does not qualitatively change the salient features of the flow and temperature fields—particularly in the deep regions (5×10^4 Pa $\lesssim p \lesssim 10^6$ Pa), discussed in this work.

We have also checked the effects of different viscosity order \mathbf{p} and coefficient $\nu_{2\mathbf{p}}$ on the flow dynamics. In general, employing higher values of \mathbf{p} and correspondingly lower values of $\nu_{2\mathbf{p}}$ (which fix the energy dissipation rate at the truncation scale) more effectively shields the large-scale flow structures from numerical dissipation and permits the overall kinetic energy spectrum to converge, as was observed in Refs. [32, 45]. In the present work, 16th-order hyperviscosity ($\mathbf{p} = 8$) is chosen because the small-scale structures in deep heating are excessively dissipated for $\mathbf{p} < 8$ and the kinetic energy spectrum is effectively same up to the dissipation scale for $\mathbf{p} \geq 8$. This is consistent with what was found in Refs. [14, 27, 29, 32].

Similarly, the timestep size Δt is adjusted when T is varied to ensure numerical stability. The Δt values in Table II (corresponding to {T341, T682, T1365} resolutions) are chosen such that the Courant-Friedrichs-Lewy (CFL) number [48] is below unity, with typical values of $\lesssim 0.2$. for the entire duration of the simulations. Finally, we have performed simulations with different values of the Robert–Asselin filter coefficient ϵ , which suppresses the computational mode from the second-order accurate leap-frog scheme employed [46, 49]. In this work, $\epsilon = 0.02$ is used because the value prevents the simulation from suffering instability while minimizing artificial damping due to its temporal smoothing. This value is consistent with that found for HD209458 b in Ref. [47].

D. Additional visualizations

A movie showing the periodic generation of large cyclonic storms from the simulation in Fig. 3b of the main

text is available at [34]. The movie shows the vorticity field ζ ($\equiv \mathbf{k} \cdot \nabla \times \mathbf{v}$, where \mathbf{k} is the local vertical direction and \mathbf{v} is the velocity field) in Mollweide map projection for WASP-96 b with deep heating. The map is centered on the substellar point, ($\lambda = 0$ and $\phi = 0$). The field at the $p = 10^5$ Pa level is shown for $t \in [125.75, 165.00] \tau$, during which ~ 13 distinct formation cycles can be seen. Additionally, Fig. 5 and 6 are high-resolution versions of Fig. 1 and Fig. 3 in the main text.

- [1] J. P. Gardner *et al.*, *Space Science Reviews* **123**, 485-606 (2006).
- [2] G. Tinetti *et al.*, [arXiv:2104.04824](https://arxiv.org/abs/2104.04824) (2021).
- [3] A. P. Showman, J. J. Fortney, Y. Lian, M. S. Marley, R. S. Freedman, H. A. Knutson, and D. Charbonneau, *The Astrophysical Journal* **699**, 564 (2009).
- [4] A. P. Showman, X. Tan, and V. Parmentier, *Space Science Reviews* **216**, 139 (2020).
- [5] E. Rauscher and K. Menou, *The Astrophysical Journal* **714**, 1334 (2010).
- [6] H. Th. Thrastarson and J. Y-K. Cho, *The Astrophysical Journal* **716**, 144 (2010).
- [7] I. Dobbs-Dixon, A. Cumming, and D. N. C. Lin, *The Astrophysical Journal* **710**, 1395 (2010).
- [8] K. Heng, K. Menou, and P. J. Phillipps, *Monthly Notices of the Royal Astronomical Society* **413**, 2380 (2011).
- [9] B. Liu and A. P. Showman, *The Astrophysical Journal* **770**, 42 (2013).
- [10] N. J. Mayne, I. Baraffe, D. M. Acreman, C. Smith, M. K. Browning, D. S. Amundsen, N. Wood, J. Thuburn, and D. R. Jackson, *Astronomy & Astrophysics* **561**, A1 (2014).
- [11] J. Y-K. Cho, I. Polichtchouk, and H. Th. Thrastarson, *Monthly Notices of the Royal Astronomical Society* **454**, 3423 (2015).
- [12] J. M. Mendonça, *Monthly Notices of the Royal Astronomical Society* **491**, 1456 (2020).
- [13] J. Y-K. Cho, J. W. Skinner, and H. Th. Thrastarson, *The Astrophysical Journal Letters* **913**, L32 (2021).
- [14] J. W. Skinner and J. Y-K. Cho, *Monthly Notices of the Royal Astronomical Society* **511**, 3584 (2022).
- [15] T. D. Komacek, X. Tan, P. Gao, and E. K. H. Lee, *The Astrophysical Journal* **934**, 79 (2022).
- [16] Q. Changeat, *The Astrophysical Journal* **163**, 106 (2022).
- [17] A. P. Showman, C. S. Cooper, J. J. Fortney, and M. S. Marley, *The Astrophysical Journal* **682**, 559 (2008).
- [18] S. Gandhi, A. S. Jermyn, *Monthly Notices of the Royal Astronomical Society* **499**, 4984-5003 (2020).
- [19] L. Wellbanks, N. Madhusudhan, *The Astrophysical Journal* **993**, 79 (2022).
- [20] Q. Changeat (private communication).
- [21] J. Y-K. Cho, H. Th. Thrastarson, T. Koskinen, P. Read, S. Tobias, W. Moon, J. W. Skinner, in *Zonal Jets: Phenomenology, Genesis, and Physics*, B. Galperin & P. Read (Cambridge University Press, 2019) pp. 104–116.
- [22] J. Y-K. Cho, *Philosophical Transactions of the Royal Society A: Mathematical, Physical and Engineering Sciences* **366**, 4477–4488 (2008).

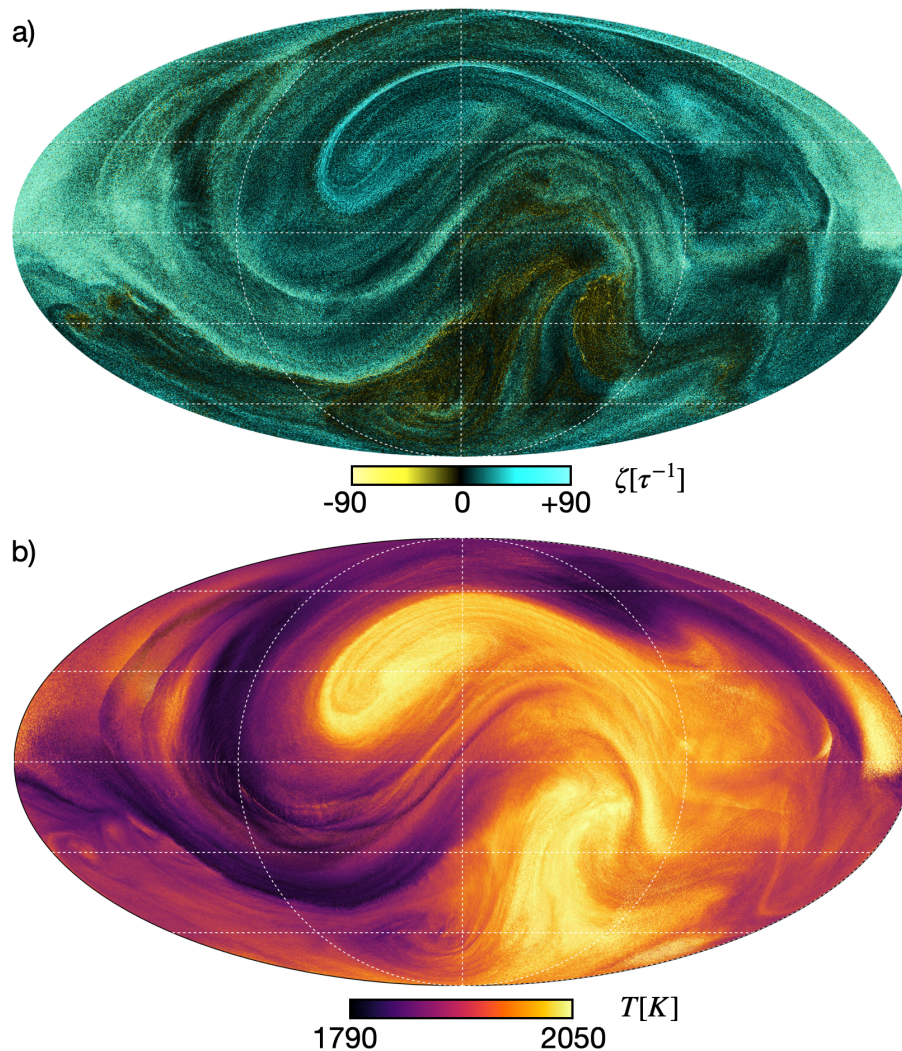


FIG. 5. High-resolution version of Fig. 1 in the main text. Vorticity ζ and temperature T fields (a and b, respectively) of a hot, 1:1 spin-orbit synchronized exoplanet atmosphere with deep heating at time $t = 155$, in units of planetary rotation period τ . The fields are in Mollweide projection, centered on the substellar point at the $p = 10^5$ Pa level; the western and eastern terminators are on the left and right of the dayside, respectively (dashed circle). The generic response to deep heating is shedding of a large vortex, spinning away westward from the substellar point to the north or south, depending on the hemisphere in which the shedding occurs. The temperature tracks the vorticity very closely. The shedding is also accompanied by *bursts* of small-scale storms and very sharp vorticity and thermal fronts, which are layered and sweeping. The overall result is a much more complex and widespread mixing of the temperature outside the vortices (as well as the usual transport in their interiors)—seen only sporadically in the atmosphere without deep heating [13, 32]. Here it is the principle state.

- [23] C. Schumacher, R. A. Houze, and I. Kraucunas, *Journal of the Atmospheric Sciences* **61**, 1341 (2004).
- [24] R. A. J. Neggers, J. D. Neelin, and B. Stevens, *Journal of Climate* **20**, 2623 (2007).
- [25] C. J. Zhang and X. Song, *Geophysical Research Letters* **36**, L09708 (2009).
- [26] M. Zhao, *Journal of Climate* **27**, 1845 (2014).
- [27] J. Y-K. Cho, K. Menou, B. M. S. Hansen, and S. Seager, *The Astrophysical Journal Letters* **587**, L117 (2003).
- [28] C. Watkins and J. Y-K. Cho, *The Astrophysical Journal* **714**, 904 (2010).
- [29] J. Y-K. Cho, K. Menou, B. M. S. Hansen, and S. Seager, *The Astrophysical Journal* **675**, 817 (2008).
- [30] R. K. Scott, L. Rivier, R. Loft, and L. M. Polvani, *BOB: Model Description and User's Guide*, NCAR Technical Notes (2004).
- [31] I. Polichtchouk, J. Y-K. Cho, C. Watkins, H. Th. Thrasartson, O. M. Umurhan, and M. De La Torre Juárez, *Icarus* **229**, 355 (2014).
- [32] J. W. Skinner and J. Y-K. Cho, *Monthly Notices of the Royal Astronomical Society* **504**, 5172 (2021).
- [33] J. C. Strikwerda, in *Finite Difference Schemes and Partial Differential Equations, Second Edition*, Other Titles in Applied Mathematics, (Society for Industrial and Applied Mathematics, Philadelphia, 2004) pp. 1 – 427.
- [34] See <https://youtu.be/oyu2glkCmGQ> and https://youtu.be/4T_noDox-0w for movies illustrating the atmospheric dynamics.
- [35] Q. Changeat *et al.*, *The Astrophysical Journal Supplement Series* **260**, 3 (2022).

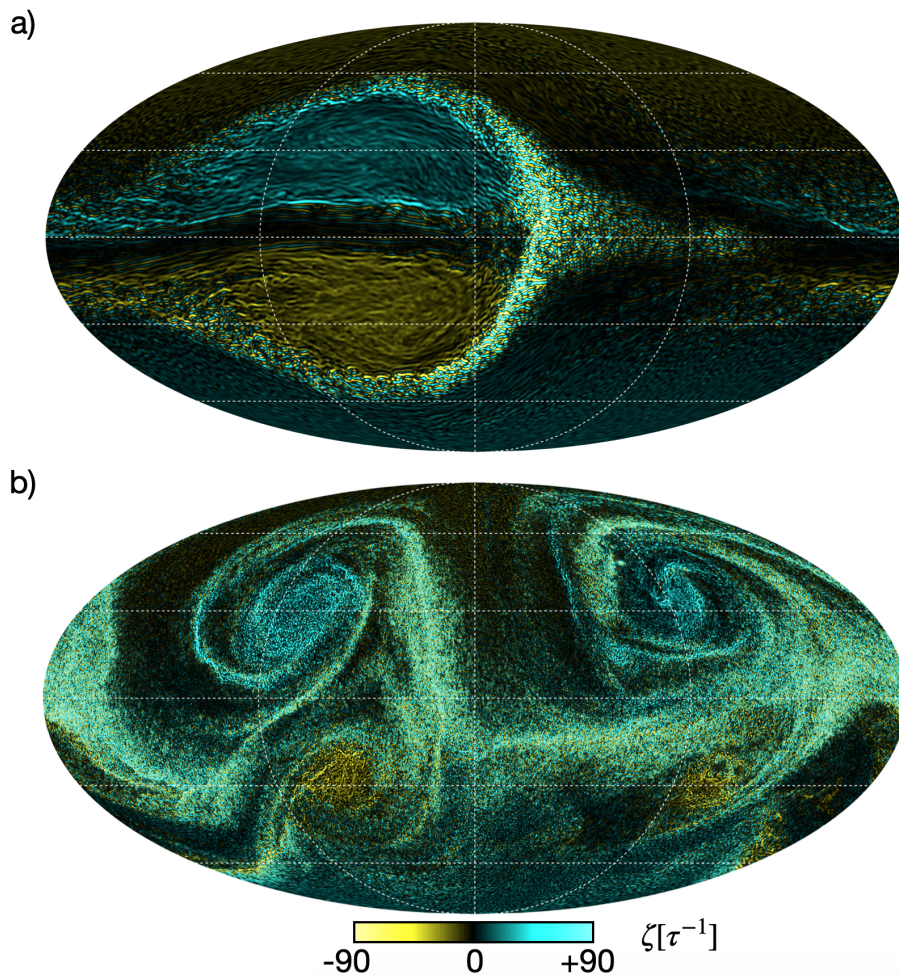


FIG. 6. High-resolution version of Fig. 3 in the main text. ζ fields at the 10^5 Pa level with shallow and deep heating (a and b, respectively), showing the flows dominated by different organized structures (after $t \approx 10$). In a) the flow is dominated by a modon and a much weaker antimodon, whereas in b) the flow is dominated by a quartet of cyclones in a von Kármán vortex street-like formation. In the latter, the cyclone quartet exhibits a quasi-periodic life cycle (of period ~ 10) that begins with the flow similar to that seen in Fig. 1a.

- [36] M. L. Salby, in *Fundamentals of atmospheric physics*, International Geophysics, Vol. 61, edited by M. L. Salby (Academic Press, 1996) pp. 321 – 340.
- [37] N. G. Hogg and H. M. Stommel, *Proceedings of the Royal Society of London. A. Mathematical and Physical Sciences* **397**, 1 (1985).
- [38] T. von Karman and H. L. Rubach, *Physikalische Zeitschrift* **13**, 49 (1912).
- [39] I. Polichtchouk and J. Y-K. Cho, *Monthly Notices of the Royal Astronomical Society* **424**, 1307 (2012).
- [40] Z. Kizner, *Physics of Fluids* **18**, 056601 (2006).
- [41] J. Rigby *et al.*, *Publications of the Astronomical Society of the Pacific* **135**, 048001 (2023).
- [42] J. L. Bean *et al.*, *Publications of the Astronomical Society of the Pacific* **130**, 114402 (2018).
- [43] Q. Changeat *et al.*, *The Astrophysical Journal Supplement Series* (2023) (accepted).
- [44] C. Hellier, D. R. Anderson, A. C. Cameron, L. Delrez, M. Gillon, E. Jehin, M. Lendl, P. F. L. Maxted, F. Pepe, D. Pollacco, D. Queloz, D. Ségransan, B. Smalley, A. M. S. Smith, J. Southworth, A. H. M. J. Triaud, S. Udry, and R. G. West, *Monthly Notices of the Royal Astronomical Society* **440**, 1982 (2014).
- [45] J. Y-K. Cho and L. M. Polvani, *Physics of Fluids* **8**, 1531 (1996).
- [46] R. Asselin, *Monthly Weather Review* **100**, 487 (1972).
- [47] H. Th. Thrastarson and J. Y-K. Cho, *Astrophysical Journal* **729**, 117 (2011).
- [48] R. Courant, K. Friedrichs, and H. Lewy, *Mathematische Annalen* **100**, 32 (1928).
- [49] A. J. Robert, *Journal of the Meteorological Society of Japan. Ser. II* **44**, 237 (1966).